Materials Today Communications 35 (2023) 105900

Contents lists available at ScienceDirect

Materials Today Communications

journal homepage: www.elsevier.com/locate/mtcomm

Characterisation of residual stresses and oxides in titanium, nickel, and aluminium alloy additive manufacturing powders via synchrotron X-ray diffraction

Max D.A. Valentine, Vimal Dhokia, Joseph Flynn, Sophie A.M. McNair, Alexander J.G. Lunt *

Department of Mechanical Engineering, University of Bath, Bath BA2 7AY, United Kingdom

ARTICLE INFO

Keywords:
Synchrotron diffraction
Additive manufacturing
Residual stress
Phase shift
Oxidation

ABSTRACT

The strength and fracture toughness of Additively Manufactured (AM) components are significantly influenced by the concentration and size of oxides and precipitate inclusions within the build powders. These features are highly sensitive to powder production parameters, as well as the number of times a powder has been reused. In this study synchrotron X-ray powder diffraction was performed in an inert atmosphere at room temperature and during in-situ heating, providing crucial insights into growth rates and distribution of oxides and precipitates as a function of temperature. From the high angular resolution data collected, the structural refinement showed that plasma wire arc atomisation shows lower residual strain than gas atomised powder samples at room temperature after atomisation likely due to lower temperatures achieved during the production process. Additionally, the results from the diffraction patterns collected during in-situ heating provide key insights to the four metal powders considered in this study, Ti-6Al-4 V, Ni718, $AlSi_{10}Mg$, and Scalmalloy. This paper also highlights the potential that using synchrotron X-ray diffraction to study AM parts and constituent AM powder has to gain crucial insight into material properties and the build reliability of end use production quality parts from AM.

1. Introduction

Metal additive manufacturing (AM) is rapidly becoming a more viable method for reliably making functional end use parts [1,2]. AM is a method of production where the final part is built up, usually layer by layer, until the final geometry has been completed. Laser powder bed fusion (L-PBF) is one method of AM that uses a laser to locally melt metal powder to build up components. The resulting parts can take advantage of the complexity to reduce the number of parts in an assembly, reduce the overall weight, or allow for increased personalisation at a larger scale of manufacturing. For these reasons, automotive, aerospace, medical, and dental industries have begun to utilise and invest heavily in the future of metal AM [3]. However, the available alloys that are suitable for L-PBF is still limited and the quality of as-built metal parts produced through AM is not yet equal to parts produced from traditional machining methods, primarily due to build defects porosity, crystal anisotropy, surface roughness, oxidation and other quality issues [4]. There is substantial potential to overcome many of these issues via refinement of powder production and printing processes, as well as post-processing. For these reasons, developing an in-depth understanding of how metal powders behave at temperature is integral in limiting the quality gap inherent to metal AM parts.

The strength and fracture toughness of additively manufactured components are significantly influenced by the concentration and size of oxides and precipitate inclusions within the build powders [5–7]. These features are highly sensitive to powder production parameters, as well as the number of times a powder has been reused [8–12]. Powders for metal AM are typically manufactured through processes called gas atomisation (GA) or plasma wire atomisation (PA) [13]. These processes work with a combination of heating up the metal wire and using a pressurised gas to create small droplets that rapidly cool into powder between 10 and 500 μm in diameter, depending on the method [14]. While gas atomisation methods rely solely on the pressurised gas, plasma wire atomisation passes the pressurised gas through an electrostatic field to produce a plasma arc, to create more uniform powders [15]. The heating and rapid cooling of the material can lead to possible defects in the powder, including surface material oxidation, non-metallic inclusions, run-to-run contamination, and internal stresses due to the rapid cooling of the material [16]. Once produced, unsintered powder in L-PBF can be reused multiple times, however, the quality of

* Corresponding author.
E-mail address: ajgl20@bath.ac.uk (A.J.G. Lunt).

https://doi.org/10.1016/j.mtcomm.2023.105900
Received 22 November 2022; Received in revised form 13 March 2023; Accepted 26 March 2023
Available online 30 March 2023

the powder degrades with further use beyond 5–10 cycles [17]. The quality degradation includes larger powder size with increased surface roughness as well as potential surface oxidation on the powders, among other factors.

Powder production methods and post processing of the atomised powder can greatly impact the quality of the powder, and therefore, the macro scale properties of the final as-built parts. Residual stress is one main L-PBF induced defect that occurs due to thermal gradients within the build chamber as a result of the layer-by-layer melting inherent to the process. Build-up of residual stresses can lead to part defects from poor mechanical properties and geometrical inaccuracies, to crack formation in the part and delamination from support structures. Residual stresses are typically greater where the part meets the substrate at the bottom of the build chamber, as the thermal conduction pathway is typically larger at the point where the part meets the build plate [18]. This is in comparison to the top of the build which is typically surrounded by unsintered powder and smaller amounts of sintered material. Large stresses must be alleviated through optimisation of the part geometry or build parameters [19,20] or through post-processing methods such as heat treatment. Untreated build-up of internal residual stresses will also hinder macro-scale properties, as Leuders et al. [21] suggest that residual stresses have a large impact on the growth of fatigue cracks. Bartlett et al. [22] presents an additional review of the impact of residual stresses on the macroscale part quality. While there is extensive literature on residual stresses developed through the L-PBF processes, it is critical to further understand the impact of these stresses in the metal powders developed through both the powder atomisation methods and by thermal cycles from powder reuse. Developing this understanding can provide greater confidence in the final part properties and methods to restore the powder quality after multiple reuse cycles.

The growth of precipitate phases and powder oxidation are additional considerations that should be monitored in the quality control of powder atomisation and in the as-built AM parts. While the volume fraction of oxides and precipitate phases are generally low, less than 2 % by weight, they can have a severe impact on the strength and fracture toughness of finished parts [23,24]. It is therefore critical to quantify how the concentration, grain size, and lattice strains of these materials are influenced by production parameters, to ensure the production of reliable components. In order to minimise oxide build up during AM, argon is used to flood the chamber during production. Despite using this approach, low levels of oxygen typically remain during the fabrication process which form oxides within the completed part and the heat-affected powder neighbouring the melt pool [25]. Isolating this powder from unaffected material is challenging, and therefore this heat-affected material is typically combined with the rest of the feedstock for use in subsequent printing. This ultimately limits the number of times a powder can be used before the mechanical performance of the resulting part degrades to an unacceptable level [8]. For this reason, improved understanding of the oxide and precipitate growth rates of both aluminium and titanium alloy powders are required at the temperatures present in these heat effected zones.

This paper focuses on four powders for L-PBF applications including titanium, nickel, and aluminium based alloys. Ti-6Al-4 V (Ti64) is a titanium based alloy whose widespread use is a result of its high specific strength, good fracture toughness, and corrosion resistance [4], which tailors it for performance components as well as medical and dental applications [17]. Alternatively, the lightweight nature and thermal properties of nickel and aluminium based alloys make it suitable for aerospace and automotive applications [17]. Ni718 is a nickel-based aerospace grade superalloy that is used for critical components such as turbine blade discs and compressor blades [17] as a result of its ability to maintain its strength and corrosion resistance at high temperatures [26]. Finally, Scalmalloy and $AlSi_{10}Mg$ are aluminium based alloys used for their good specific strength properties and manufacturability, allowing for easier post-processing [27].

In this study, synchrotron X-ray powder diffraction (XRD) is performed at room temperature and during in-situ heating to provide crucial insights into growth rates and distribution of precipitates and oxides as a function of temperature. Additionally, the XRD patterns will offer a better understanding on the internal stresses that are a result of the powder fabrication process, and how these stresses develop and behave at increasing temperatures. Through investigating Ti-6Al-4 V, Ni718, Scalmalloy, and $AlSi_{10}Mg$ powders, these results will facilitate the optimisation of production parameters and provide the critical insights required to maximise powder reuse while conserving mechanical performance over extended periods of time and reuse cycles.

2. Material and methods

2.1. Materials and sample preparation

A range of metal powders commonly used in AM were supplied by Carpenter Technology (Liverpool, United Kingdom). Following production, sieve analysis is performed on the powders by this manufacturer to ensure that powders only within the desired range (30–60 μm in diameter) are distributed for use. Tables 1–4 detail the chemical composition of the four materials, as specified by Carpenter Technology [28–31]. Example images of the morphologies of these powders are also available on the datasheets linked in these references. The powders were produced through a specification gas atomisation, and one additional sample of Ti-6Al-4 V was produced through plasma wire atomisation for comparison.

2.2. Synchrotron diffraction

The synchrotron diffraction data collection was conducted using the Beamline I11 at Diamond Light Source in the United Kingdom [32]. The beamline uses Mythen sensors with a high angular resolution (0.004°) to record diffraction patterns up to a rate of 1 kHz. This is significantly faster than the hours required from traditional or lab-based equipment [33]. The combined high energy, and high temporal resolution means that this approach has significant potential to improve existing understanding of additively manufactured parts and powders [34,35]. Synchrotron diffraction is an analytical method of using incident energy radiation to measure characteristic diffraction patterns to determine the crystalline structure of a specimen. These patterns are a result of constructive interference which can be described by Bragg's Law, $\lambda = 2d\sin\theta$, which relates the lattice planes spacing of the medium of interest to (d) to the scattering angle (2θ) via the wavelength of the incident X-rays (λ) [36]. By analysing the scattering angle using X-rays of known energy, it is possible to quantify the average lattice spacing between planes in polycrystalline materials, which is a direct measure of strain (and thereby stress) in the powders.

Synchrotron facilities provide crucial opportunities to gain key insights into the structural characteristics of materials without the need for destructive testing of parts. While XRD has been used in a wide variety of applications [37–39], the properties of synchrotron radiation mean that it has increasingly become beneficial in the characterisation of AM parts and the constituent powder. In particular, the high energies of synchrotron sources can be used to probe heavier elements such as those used in metal AM [40], the detectors within these facilities provide greater angular resolution (and thereby provide more precise strain estimates) [33] and in-situ analysis can be performed due to the high frame rates that can be achieved (up to 700 Hz) [33]. There are also added benefits in being able to perform transmission mode XRD and record accurate measurements at elevated temperatures [40,41]. The purpose of this study is to exploit the latter of these benefits, in order to provide insight into the high temperature characteristics of AM powders, during in-situ heating in order to better understand stress evolution and phase growth.

Table 1
Chemical composition of Ti-6Al-4 V (mass percent, %) (Carpenter Technology, Liverpool, United Kingdom) [28].

Ti	Al	V	Fe	O	C	N	H	Y
Balance	5.50–6.50	3.50–4.50	< 0.25	< 0.13	< 0.08	< 0.03	< 0.0125	< 0.005

Table 2
Chemical composition of Ni718 (mass percent, %) (Carpenter Technology, Liverpool, United Kingdom) [29].

Fe	Cr	Mo	Co	Si	Cu	Ni	P	B
Balance	17.0–21.0	2.80–3.30	1.00	< 0.35	< 0.30	< 0.03	< 0.015	< 0.006
Ni	Nb	Ti	Al	Mn	C	O	S	
50.00–55.00	4.75–5.50	0.65–1.15	0.20–0.80	< 0.35	< 0.08	< 0.03	< 0.015	

Table 3
Chemical composition of $AlSi_{10}Mg$ (mass percent, %) (Carpenter Technology, Liverpool, United Kingdom) [30].

Al	Fe	Sn	O	Cu	N	Sc
Balance	< 0.55	0.20–0.45	< 0.10	< 0.05	< 0.05	0.05
Si	Mn	Ti	Pb	Ni	Zn	
9.00–11.00	< 0.45	0.15	< 0.10	< 0.05	< 0.05	

Table 4
Chemical composition of Scalmalloy (mass percent, %) (Carpenter Technology, Liverpool, United Kingdom) [31].

Al	Mg	Zr	Si	Ti	O
Balance	0.60–0.88	0.20–0.50	< 0.40	0.15	< 0.05
Sn	Mn	Fe	Pb	Cu	
4.00–5.10	0.30–0.80	< 0.40	< 0.25	< 0.10	

2.3. Experimental setup

This experiment focused on four commercially available, commonly used AM powders composed of 30–60 μm diameter particles. Synchrotron X-ray powder diffraction was used to determine the crystal structure of the powders at the I11 beamline at Diamond Light Source, UK. Beamline I11 generates synchrotron radiation via an in-vacuum undulator (U22) inside the main electron storage ring to produce an X-ray beam with an energy range of 5–30 keV, with a peak flux at 15 keV [32]. Energy selection for the experiment was performed by varying the incident wavelength and maximising the scattered signal. This analysis demonstrated that despite a minor increase in transmission length at higher energies, the reduction of incident flux resulted in an overall reduction in scattered signal. For this reason, a 15 keV monochromatic beam with a wavelength of 0.82644 Å, was used throughout the experiment, which led to patterns with maximum peak intensities of over 100,000 counts for all samples. Calibration of the synchrotron radiation and sample to detector distance was completed using a silicon sample (SRM 640c, US-NIST). This also provided a quantitative value for the zero point (0.00162(2)°) which is the offset between the detector motor reading and the true value of direct beam, which was subsequently corrected for in all of the data collected. Instrument broadening was determined from this diffraction pattern and was corrected via the use of the XRD processing package DAWN [42]. A beam size of 0.75 × 1 mm (vertical × horizontal) was selected to ensure complete illumination of the samples. The rapid cooling associated with the production of these particles ensures that 30–60 μm spherical particles are nanocrystalline, which means that 10^{11} particles or 10^{22} grains were nominally illuminated in each sample.

The powder samples were loaded in 0.5 mm diameter capillaries made of quartz and were transferred from a carousel to the capillary spinner on the diffractometer using a robotic arm. A magnetic capillary mount was used to ensure that the sample and calibrants were mounted to nominally the same position (within a few microns). This process ensured the samples are placed consistently relative to the beam compared to the Si calibration sample. Time resolved XRD patterns were recorded using the wide-angle position sensitive detector (PSD). The PSD has an aperture of 90°, therefore the diffraction data was measured from 0° to 90° (2θ) with an angular resolution of 0.004°. Optimisation of the exposure time was performed to obtain diffraction patterns with signal intensity sufficient to reliably fit the diffraction peaks, which was found to be 60 min per sample. The PSD comprises of Mythen-2 silicone μ-strip modules mounted on the δ-circle, which acts around a central axis horizontally and perpendicular to the incident beam as shown in Fig. 1. High resolution measurements were also recorded using 5 multi-analysing crystal (MAC) devices. Further information on the technical operation is provided by the I11 beamline facility website [43].

High quality x-ray diffraction patterns of the samples were recorded at both room temperature (RT) and high temperatures (HT). RT powder characterisation was collected on the samples specified in Table 5 for an hour using the MAC detectors to exploit the higher angular resolution of this arrangement (1×10^{-5} °). 1D intensity vs 2θ diffraction patterns

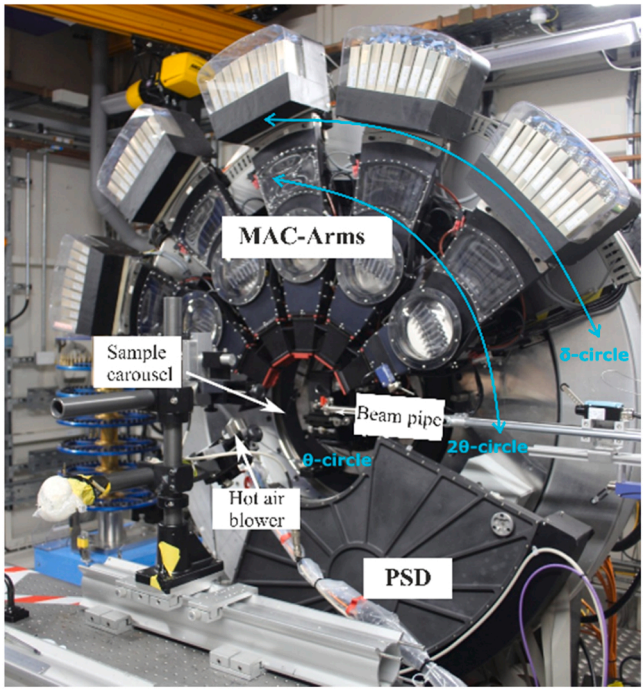

Fig. 1. XRD experimental setup of the I11 beamline at the Diamond Light Source [43].

Table 5
RT AM Powders.

#	Metal	Atomisation Method
1	Ti-6Al-4 V	Gas atomised
2		Plasma wire
3	Ni718	As produced
4	$AlSi_{10}Mg$	Gas atomised
5	Scalmalloy	Gas atomised

were collected in the 2θ range from 5° to 95°. A decision was made to use the PSD was selected for the remaining HT-XRD due to the substantially longer exposure times associated with the MAC detectors (1 h vs 5 mins for the PSD). The reduced exposure times of the PSD ensured that the transient effect of heating and holding the powder at temperature were minimised in the diffraction patterns, at the cost of reduced angular resolution (0.004°).

For HT characterisation, the Cyberstar hot air blower (Cyberstar, Grenoble, France) was mounted onto the XYZ table and the low-pressure gas cell was used to evacuate the capillaries. Calibration of the hot air blower was performed using a platinum sample (99.95 % pure 45 μm diameter powder from Goodfellow). X-ray diffraction patterns were collected from this sample at room temperature and by setting the air blower to four temperature increments from 200 °C to 800 °C (20 min, exposure time). The thermal expansion characteristics of Pt have been precisely determined [44] and therefore, by fitting these patterns and determining the corresponding lattice spacings, precise estimates of the sample temperature could be determined for each air blower set point. The differences between the set hot air blower temperature and the sample temperature were then subsequently used to calibrate the system and ensure the sample temperatures applied throughout the HT characterisation were precise and reliable.

For this experiment, the samples were heated from room temperature at a rate of 10 °C/min and were subsequently held at the holding temperatures specified in Table 6 for 30 min each. After the initial hold temperatures, the heating process at a rate of 12 °C/min leading into the final hold temperature was recorded. In-situ heating of the powder samples while collecting XRD patterns was performed to monitor structural changes as a function of time. Although capillary spinning is not possible in this configuration, sample rocking over ± 5° was performed to improve averaging. The high temperature synchrotron XRD was performed from 2θ angles of 5–75°. Between each sample, dark field correction was performed by collecting patterns with the shutter closed, and flat field correction was implemented by collecting patterns of an empty capillary. The temperature ranges in Table 6 were chosen to simulate the heat affected zones present in unsintered powder near the laser of each of these materials. For titanium and nickel powders this temperature can reach up to 700 °C [45,46], however in general 500 °C is the maximum value achieved for aluminium alloys [47]. It should be noted that a higher starting temperature was selected for the titanium alloy (200 °C) due to its increased resistance to oxidation at these relatively low temperatures [48].

2.4. Data processing

Structural analysis of the XRD patterns was completed using the rietveld refinement method [49] on TOPAS [50]. To fit the analytical structure to the collected XRD patterns, constituent phases of the AM powder were identified by comparing the characteristic diffraction patterns to various online databases (including the Crystallography Open Database (COD) [51–53] and Inorganic Crystal Structure Database (ICSD)). With the input structure of the present phases of each material sample, Rietveld refinement was used to gain quantitative information on the powder samples at each temperature. This provided the lattice parameters and relative weighting of each phase to be identified. Rietveld refinements work by using the least squares method to match the structural intensity, point-by-point, to the collected XRD data [54]. This entailed refining specific properties including a background fit (characteristic to the radiation and instrument), material radiation absorption, crystal lattice geometry and parameters, constituent phase weight percentage, and crystal lattice strain. The datasets at each temperature were refined sequentially, first by obtaining an adequate fit for the first timestep of each temperature dataset, and then refining the structure for following timesteps based on the previous refined crystal structure. This provided information on how the crystal structure and size, phase microstrain, and phase weight percentage developed over time for each sample.

Table 6
Temperature of HT studies.

Sample #	Hold Temperature (℃)							Ramp Temperature (℃)
1	200	300	400	500	600	700	–	200–700
3	100	200	300	400	500	600	700	100–700
4	100	200	300	400	500	–	–	100–500
5	100	200	300	400	500	–	–	100–500

In this experiment, detailed Rietveld refinement was initially completed at room temperature and then used as the baseline structural parameters for the further sequential analysis at the specified elevated hold temperatures. Evolution of the lattice spacing can be used to quantify thermal expansion properties, as thermal excitation leads to changes in spacing between crystallite planes that can be quantified via XRD [55–57]. This measure can also be used to probe along with lattice strain and the corresponding relaxation typically observed at higher temperatures. The phases present within the powder material are also provided by matching the peaks in the XRD data to known crystal structures. By identifying these peaks, the material phases present in the sample were confirmed and therefore used throughout the sequential refinement to evaluate the evolution of precipitate phase weight percentages as the sample was held at specified temperatures over time. Structural refinement method also provided a weighted residual percentage for any given dataset which quantifies how close the analytical structure matches the sample synchrotron data. Each structural fit was accepted based on its goodness of fit (GoF), which is a ratio of the expected residual value to the weighted residual value of the pattern. Individual refinement data was only accepted with GoF values of 5 or below. Due to the high precision of the diffraction data and the large number of refinements, this value was higher for some of the high temperature sequential refinements. Confidence intervals for each of the fitted values were obtained from the refinement process, and error bars equal to the standard deviation have been included in all plots.

3. Results and discussion

3.1. Room temperature analysis

Room temperature analysis of the powder samples was conducted to gain both a baseline of the constituent phases in the four materials, and to compare atomisation methods in the production of Ti64 powder. Room temperature synchrotron XRD patterns were collected for the Ti64 that had been produced by both gas atomisation and plasma wire atomisation. While gas atomisation is more common due to its cost and speed, the precision and quality of powder made by plasma wire atomisation can be seen to be better in terms of its particle sphericity and volume consistency [13,17]. Additionally, the gas atomised samples had a higher induced thermal strain during its production than the plasma wire atomisation samples as a result of less uniform rapid cooling of the powder [8,10,58].

The XRD patterns of both GA and PA room temperature samples of Ti64 indicate thermal strain, which are most clearly shown at low scattering angles (Fig. 2). This phenomenon is present across the entire spectra but the angular shift caused by the same amount of lattice strain

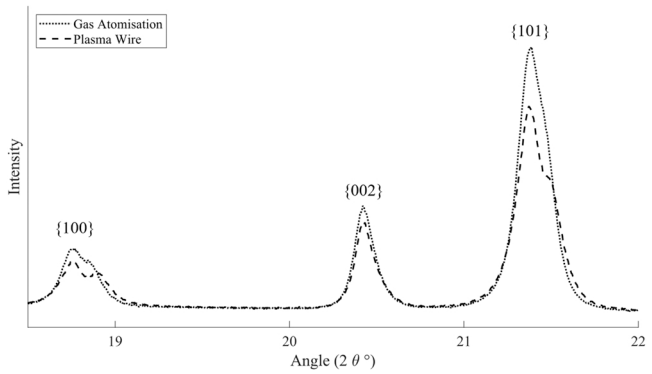

Fig. 2. XRD pattern of Ti64 sample produced through gas atomisation and plasma wire atomisation.

is larger at smaller scattering angles, so is most visible in the first few peaks. The first and third peaks of the α titanium phase ({001} and {101} at roughly 18.8° and 21.4° respectively) demonstrate broad peaks and peak splitting in both samples; however, it is much more pronounced in the gas atomised sample. This is an indicator of two distinct stress states and lattice spacings present in the powder particles. It is important to note that reduced peak splitting is observed in the {002} peak at approximately 20.5°. This difference arises from the high anisotropic crystalline stiffness within the alpha phase Ti64, which is known to resist deformation in this Miller index direction [59].

The origin of this difference can be explained by the production process. The atomisation forms a spherical particle of molten metal. The solidification front starts on the edge of the sphere and moves towards the centre. This leads to the outer shell solidifying first, and subsequently being pulled inwards by the cooling and shrinking inner core. This puts the outer surface into compression and the core into tension [60], as illustrated in Fig. 3. Albu et al., 2020 also found that this presence of well-defined peak splitting, as is seen in the first and third peak of the GA sample (Fig. 2), may be evidence of the high cooling rate of the powder during production [61]. This effect is exaggerated with materials that have a higher thermal expansion coefficient and when the atomisation method produces larger powder particle volumes, as can be the case in gas atomisation [16].

3.2. Ti-6Al-4V

3.2.1. Phase characterisation

Ti-6Al-4 V (Ti64) is a two-phase alloy containing an α and β titanium phase. At lower temperatures, the α phase is more prominent, and the mix of the two becomes prominent and measurable as the temperature increases [62]. Pederson et al. (2003) found evidence of phase transformation at 710 °C, with the phase content decreasing to unobservable levels at hold temperatures of 795 °C and 900 °C. The α phase is a hexagonal lattice structure (P63/mmc space group) with lattice constants a= 2.917260 Å and c= 4.661800 Å. The β phase was not observed in the initial XRD scans and is typically not found in virgin Ti64 powder. However, with increased powder reuse involving rapid cooling in the build chamber, Montelione et al. (2020) found that it will form in between the grains of the martensitic α phase [12]. The synchrotron XRD pattern at room temperature for this alloy is shown in Fig. 4 and was used to confirm the phase composition of this powder sample, where only peaks of the α phase can be identified. It should be noted that in order to achieve effective refinement and fitting of the diffraction pattern, two different alpha phases were required, one which was alpha phase in with an increase in lattice spacing (Ti(1)) and the other which was alpha phase with a reduction in lattice spacing (Ti(2)). As outlined in detail above, this is associated with the peak splitting and two distinct stress states within the powder. The peaks in Fig. 4 are labelled with their corresponding phase and reflection plane.

Fig. 5 shows the observed synchrotron XRD patterns at each of the hold temperatures recorded for this sample. At all temperatures, the α phase remains the dominant phase with very as has previously been observed in the literature [63]. However, at 700 °C the growth of a new phase can be observed, as outlined in more detail in Section 3.2.3.

3.2.2. Thermal expansion and stress relaxation

As the powder sample is heated up, the crystal structure expands as evidenced by the increasing lattice parameters in Fig. 6. This corresponds to the XRD peaks shifting towards lower 2θ angles in Fig. 5. At low temperatures (below 500 °C), as expected, the lattice parameters increase linearly with respect to the temperature increase ($\approx 6 \times 10^{-5}$ °C^{-1} and $\approx 1 \times 10^{-4}$ °C^{-1} for the a and c lattice parameters respectively). However, in the Ti64 sample, as the temperature increases beyond 500–600 °C, the trend deviates from this linear behaviour demonstrating that an additional structural change has occurred.

A possible explanation of this shift is a result of stress relaxation in the powder grains, as the elevated temperature allows for thermal stresses in the production method to be relieved. While thermal expansion is one explanation of peak shifting, another is strained crystallite grains. When an entire sample has strained particles or grains, it will shift the diffraction peaks from the location corresponding to the unstrained lattice parameter. Therefore, as the sample reaches adequate temperatures to relieve the internal stress, the peaks will trend back towards their initial unstrained positions (Fig. 6) [40]. It is important to highlight that in general heating of samples can also lead to peak shift due to diffusion and chemical composition changes, however the production processes used within these samples have been intentionally designed to provide a homogenous elemental composition, so this effect is unlikely to be an influential factor.

The Ti64 as-processed powder showed large degrees of peak splitting (Fig. 5), which is evidence of high levels of lattice strain in the sample. Therefore, to visualise the evolution of peak splitting as the sample was heated, the refinement pattern was fitted with a structure that accounted for peak splitting by modelling single peaks as two constituent peaks. The lattice parameters with two split peaks of the same alpha phase are shown in Fig. 6. At low temperatures, the difference in lattice parameter

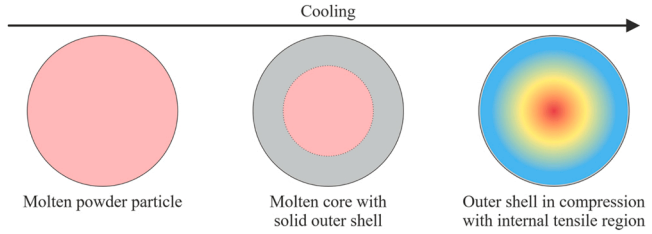

Fig. 3. Internal stress development of atomised metal powder grains.

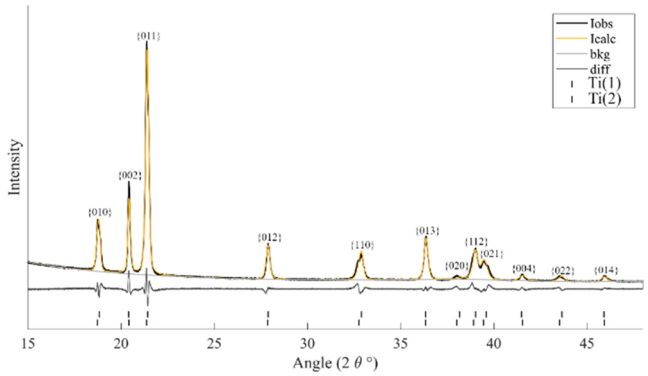

Fig. 4. Full room temperature XRD pattern of gas atomised Ti64.

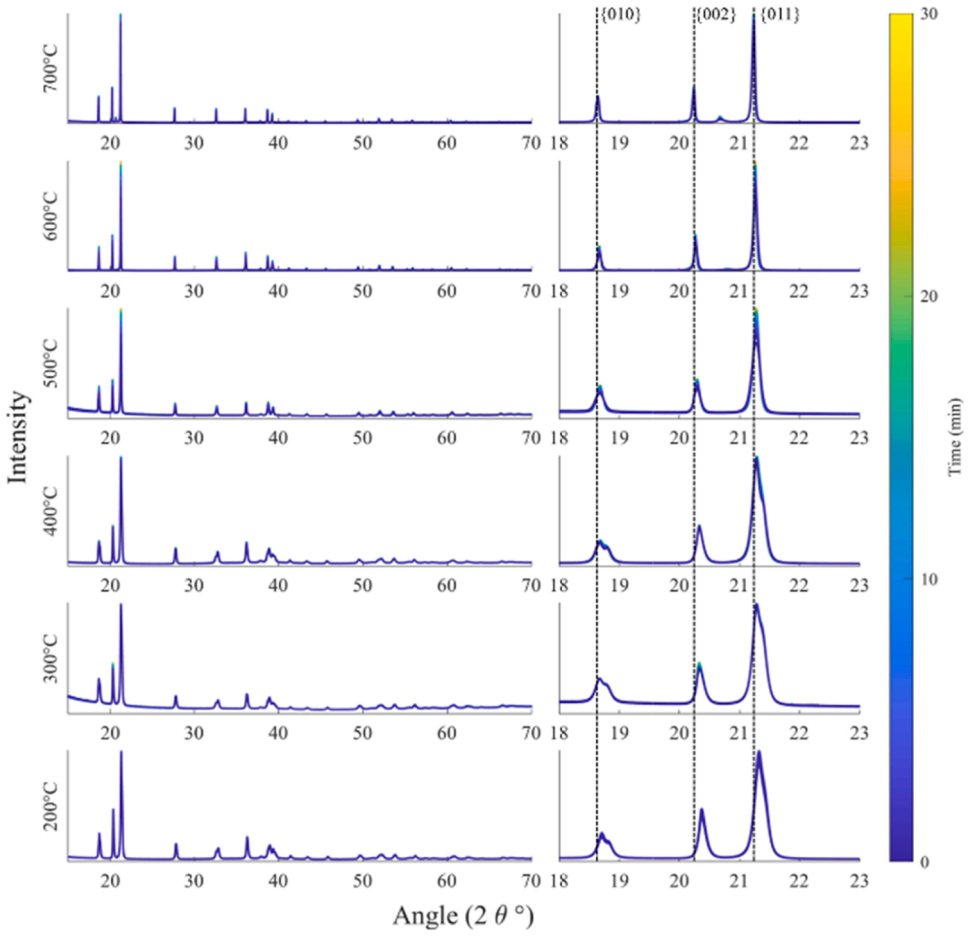

Fig. 5. Full (left) and low angle (right) XRD patterns from 200 °C to 700 °C of Ti64 sample.

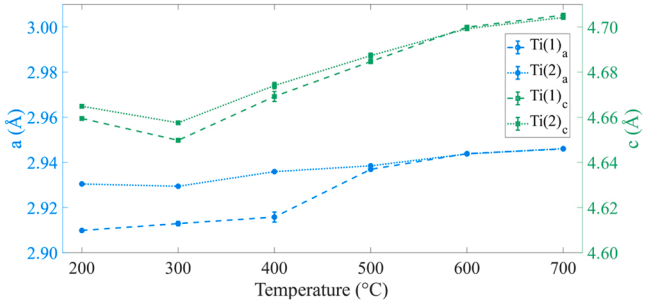

Fig. 6. Lattice parameter expansion of Ti64 showing strain relief.

for this phase is a result of strain induced peak splitting. As the temperature was beyond 500 °C, the peak locations converged, suggesting a lower degree of lattice strain as the peak splitting is eliminated. Fig. 6 also highlights that the differences between the alpha phase in tension Ti (1) and alpha phase in compression Ti(2) are more pronounced for the a lattice spacing than for the c. This is a direct result of the anisotropic crystalline stiffness of Ti64 [59], in which the stiffness of the unit cell in the c direction is substantially higher than in the a direction. Accordingly, for the same applied stress, the change in lattice spacing is higher in the a direction than in the c. This also directly corresponds to the reduced peak splitting observed on the {002} peak (oriented along the c axis), when compared to the peak splitting observed in the {100} direction (oriented along the a axis).

The peak width can also be used to infer the strain of the powder grains. The principal benefit of this measure of strain is that it is independent of temperature, meaning that it can be used to directly compare strain relief without the need to know the precise thermal expansion of the lattice which is typically unknown a priori (as in this case). Accordingly, it has found widespread use as a quantitative measure to infer strain changes in thermal XRD studies in the past [64–66]. Fig. 7 shows the trend of the microstrain broadening with increasing temperature from the HT-XRD structural refinements. Microstrain broadening is a parameter that is obtained from peak fitting and represents the distortion or lattice strain within the crystallites being characterised [64–66]. It has a maximum value of 10,000 nm and a minimum value of 0 nm which indicate highly distorted (strained) and

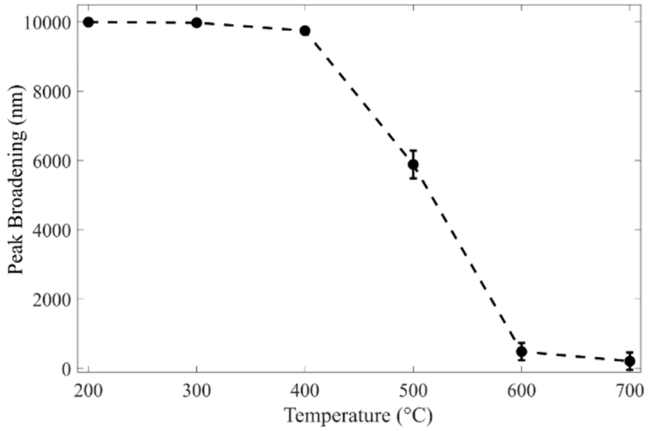

Fig. 7. Microstrain broadening of Ti64 powder.

perfectly undistorted (unstrained) crystallites within the gauge volume, respectively. As the peak splitting reduced and the peak locations trended to their unstrained positions, the microstrain broadening (and shape of the peaks narrowed) which is indicative of lattice strain relief.

3.2.3. Oxide growth

Although performed in an inert atmosphere, there are potential signs of oxidation in the diffraction patterns at high temperatures. This oxygen is likely trapped in the particles during production or via trace amounts in the inert atmosphere, however oxidation growth is something that should be avoided and eliminated where possible. Fig. 8 shows the synchrotron HT-XRD as the powder is heated from room temperature up to 700 °C. Along with the peak shifting and decreasing peak widths, there is an additional peak that grows at roughly 2θ= 21° that appears between 600 °C and 700 °C. As the powder is held at 700 °C, it continues to grow. According to analysis by Malinov et al. [40], this peak may be a result of the α phase oxidising at the surface of the powder grains. Although this is a potential response, it should be noted that there is a chance that this peak may also correspond with the growth of the β{110} peak [10,40]. A further focused study on this phenomenon would be required to distinguish between the two origins of this effect, which goes beyond the focus of this present study. Accordingly, the low weight concentrations of these elements meant that fitting could be performed with either phase, but with a low level of confidence. The lack of confidence in this result has meant that it has not been reported here, but in either case, the growth of this phase is detrimental to part mechanical performance and therefore should be avoided where possible.

3.3. Ni718

3.3.1. Phase characterisation and transformation

Ni718 is a superalloy that has a large range of applications due to its favourable physical properties arising from the mixed constituent phases within the alloy. Ni718 is a mix of γ and γ'' phases, with the γ'' phase allowing for the strength hardening of the bulk material. However, at high temperatures, the γ'' phase tends to dissolve into the δ phase precipitate, which has been found to lower the bulk material's ductility and reduce overall mechanical response [67]. The room temperature synchrotron XRD patterns of the Ni718 sample in Fig. 9 shows the main γ phase as the dominant peaks. The refinement results showed evidence of the secondary γ'' phase increasing in weight percentage from 400 °C and above, increasing from 10 % (± 0.5 %) at 100 °C up to 20 % (± 5 %) at 500 °C. However, this phase shift is difficult to see in the full diffraction pattern due to the prominence of the base γ phase. The base γ phase has a cubic lattice structure with space group Fm-3 m and lattice constant a= 3.601352 Å at room temperature. As the sample is heated in-situ, further phase transformation occurs from the γ'' dissolving into the δ precipitate from 500 °C.

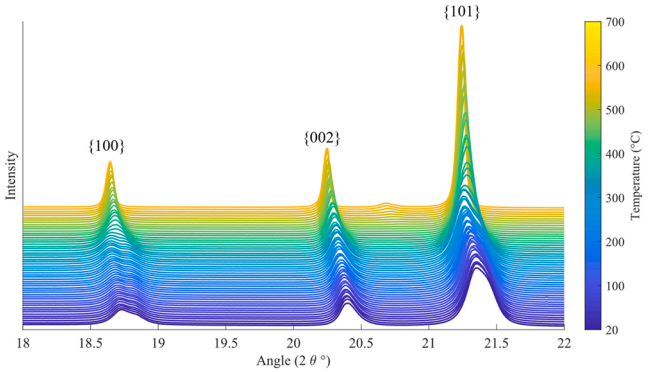

Fig. 8. Low angle diffraction pattern of in-situ heating of Ti64.

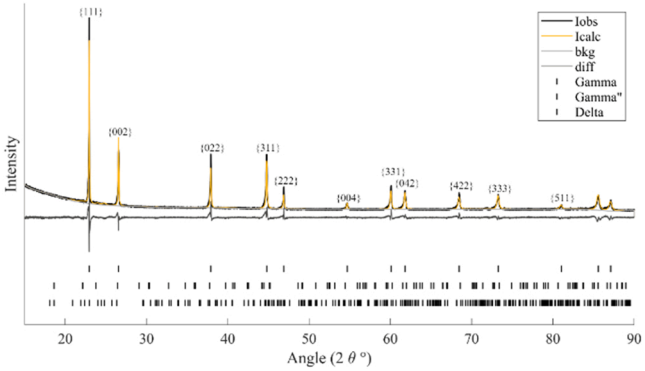

Fig. 9. Room temperature XRD pattern of Ni718.

3.3.2. Thermal expansion and stress relaxation

In the case of Ni718 it can be seen that there is significant asymmetry in the shape of the diffraction peaks at lower temperatures (Fig. 10). This is indicative of the residual stress/strain within the particles that have been induced by the production process, as has been observed widely in the literature [68–70]. Peak asymmetry is indicative of the relative magnitude and volumes of stress within the gauge volume, which are indicated by two distinct features. The magnitude of stress / strain is associated with the shift of one side of the peak away from the unstrained peak centre, whereas the volume of material at a particular stress state is associated with the peak intensity at this location. These two factors can be combined together to provide a compatible stress state which generates an asymmetric peak. In this case, the tail observed to the left of the peak suggests that there is a high magnitude tensile stress present within a smaller number of grains (large shift, low intensity), which are balanced by a lower magnitude compressive stress in a larger number of grains (small shift, large intensity). The peak asymmetry factor [71] of 1.47 at room temperature reduces but remains at 1.19 at 700 °C suggesting that complete stress relief is not achieved via annealing even at these temperatures.

Peak shifting of the γ phase peak centres is also induced via thermal expansion, and this shift is linear until roughly 400 °C, at a rate of 2.6×10^{-3} Å^3 °C^{-1}. Fig. 11 illustrates where the deviation from the linear trend occurs, as the lattice strain is partially relaxed. Despite the large initial offset from the trend at 500 °C, it can be seen that a line with identical gradient but offset from the initial linear relationship, fits the data within the confidence limits obtained. This type of offset is characteristic of annealing and strain relaxation within the cell [72,73]. Unlike other materials, the low thermal conductivity and high temperature mechanical performance of Ni718 means the material must be held at a high temperature for an extended period to fully relieve the lattice strain.

3.4. $AlSi_{10}Mg$

3.4.1. Phase characterisation

$AlSi_{10}Mg$ is comprised of two main phases; the dominant phase is α-Al into which fine fibrous Si is precipitated [61,74,75]. At room temperature the α-Al has a cubic lattice structure with space group of Fm-3 m where a = 4.045659 Å and the Si phase is also cubic with a space group of Fd-3 m and a = 5.436229 Å. Fig. 12 shows the room temperature synchrotron XRD pattern of the powder with the phase peaks labelled. Fig. 13 shows the synchrotron XRD patterns as the material is heated from 100 °C to 500 °C. At room temperature, the material consists of 7.58 % Si phase, demonstrating that the rapid quenching of the particles did not allow sufficient time for alpha phase precipitation to the nominal percentage expected at this hypoeutectic weight percentage (31.1 %). As the system reaches 500 °C, and gets close to the eutectic temperature of this system (575 °C) diffusion effects

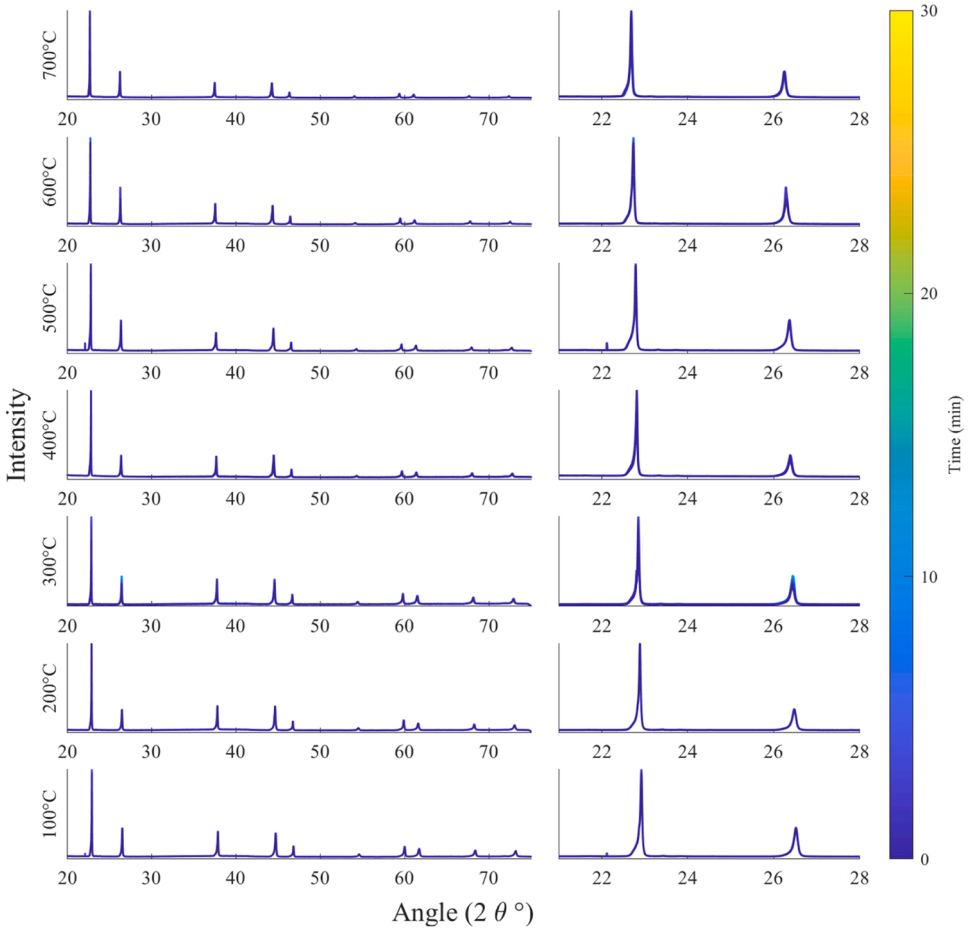

Fig. 10. Full (left) and low angle (right) XRD patterns of Ni718 at hold temperatures from 100 °C to 700 °C. Peak asymmetry is observed due to the residual strains within the powders.

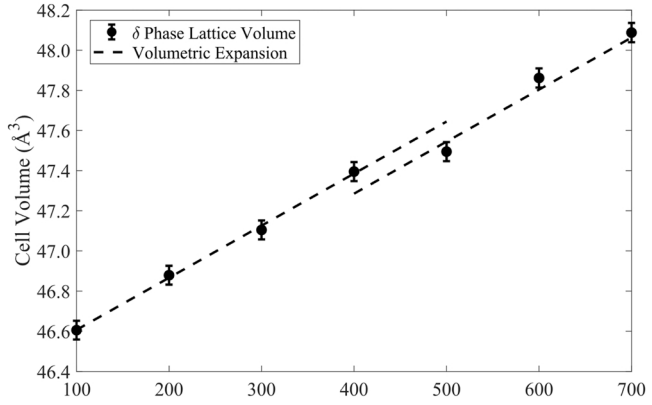

Fig. 11. Lattice cell volume of main Ni718 phase as hold temperatures are increased.

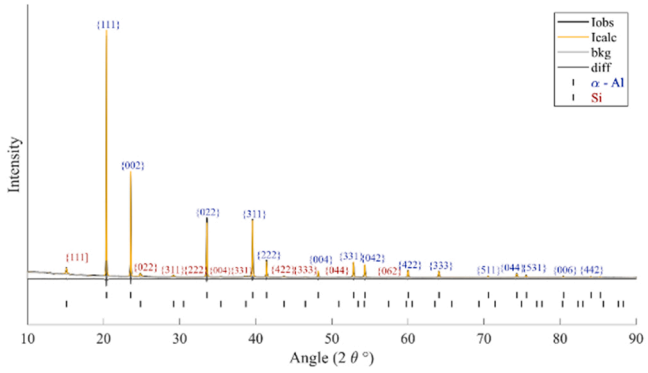

Fig. 12. Full room temperature XRD pattern of $AlSi_{10}Mg$.

become sufficient to facilitate growth of the alpha phase (towards 31.1 %), with the nominal percentage found to be 13.65 %. This is clearly shown in the narrowing and intensity growth of the {111} and {022} reflections of the Si phase in Fig. 13b.

3.4.2. *Thermal expansion and stress relaxation*

The thermal expansion of aluminium based alloys is evident in the peak shifting. Additionally, much like the Ni718 powder samples, at low temperatures the peaks have a distinctive tail to the low 2θ angle side of the peaks. The characteristic thermal properties of aluminium mean this stress induced asymmetry is relieved at lower temperatures, however this is difficult to see through changes to the linear trend in thermal expansion (Fig. 14). These thermal properties also form the basis of the degree of peak shifting in the synchrotron XRD patterns. The peaks narrow as the sample increases in temperature, demonstrating that residual stresses from the atomisation process are being relieved at higher temperatures. (Fig. 15).

3.5. *Scalmalloy*

3.5.1. *Phase characterisation*

Although the chemical composition of Scallmalloy is similar to

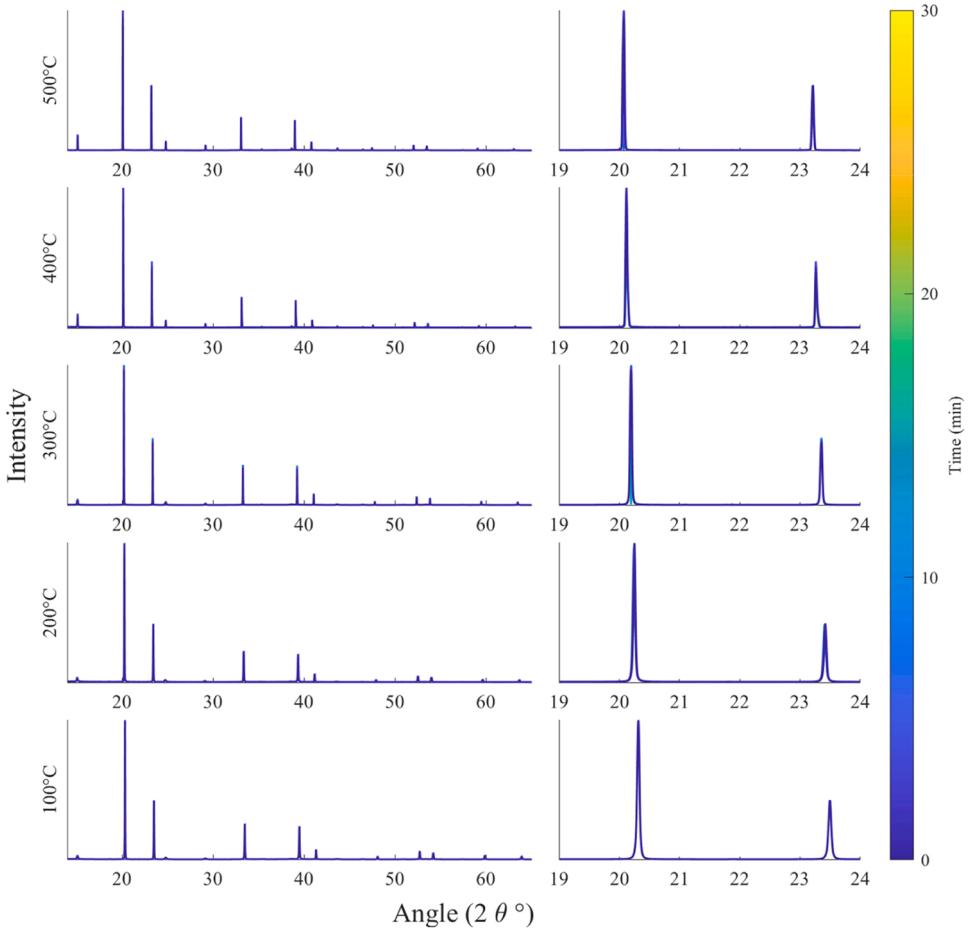

Fig. 13. Full (left) and low angle (right) XRD pattern of $AlSi_{10}Mg$ at each hold temperature from 100 °C to 500 °C.

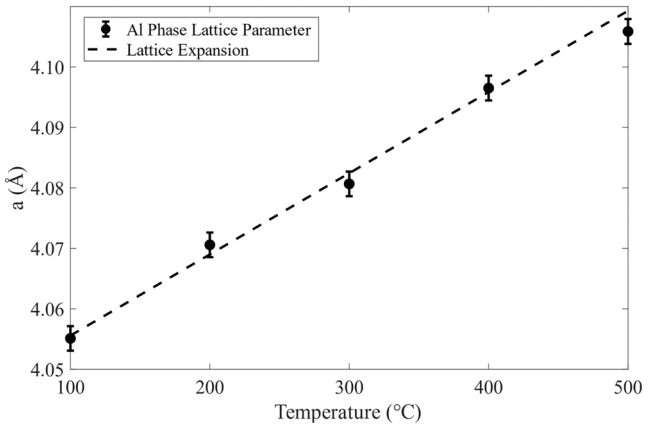

Fig. 14. Lattice parameter expansion as hold temperatures of $AlSi_{10}Mg$ are increased.

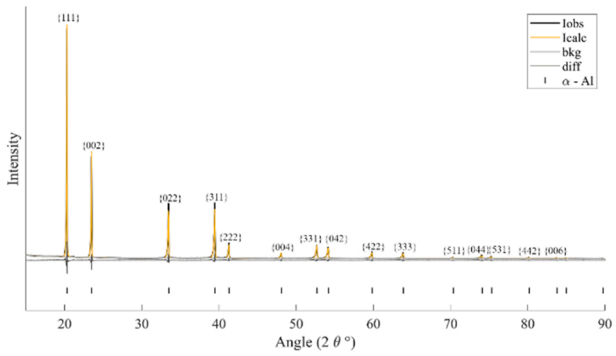

Fig. 15. Full room temperature XRD pattern of Scalmalloy.

$AlSi_{10}Mg$, the microstructure does not contain any Si precipitates (Fig. 16). At room temperature, the α-Al phase has the same cubic Fm-3 m lattice structure as $AlSi_{10}Mg$ above, however the lattice is larger, a = 4.057605 Å. There are no signs of oxidation or phase changes through the 500 °C temperature range measured of this material. While aluminium alloys have a propensity towards oxidation and forming Al_2O_3 on the surface would not be unsurprising, it is not evident in the Scalmalloy sample. Cordova et al. demonstrated this after three reuse cycles, the Scalmalloy powder still has a low oxygen ratio and it keeps its purity due to the stabilising elements present [8].

3.5.2. *Thermal expansion and stress relaxation*

The production of this sample left with high residual strains, as shown by the large degrees of asymmetry at low temperatures (Fig. 16). Unlike Ni718, however, this asymmetry is greatly reduced as the material is heated. The thermal expansion follows a linear trend up until 300 °C, where the peaks can also be seen to trend towards a more symmetrical shape in Fig. 16. As the lattice expands and the peaks shift towards lower angles, the asymmetry trending towards uniformly shaped peaks is illustrating the stress relief in the lattice. Until this point at 300 °C, the coefficient of thermal expansion is approximately 1.70×10^{-4} °C^{-1} (Fig. 17).

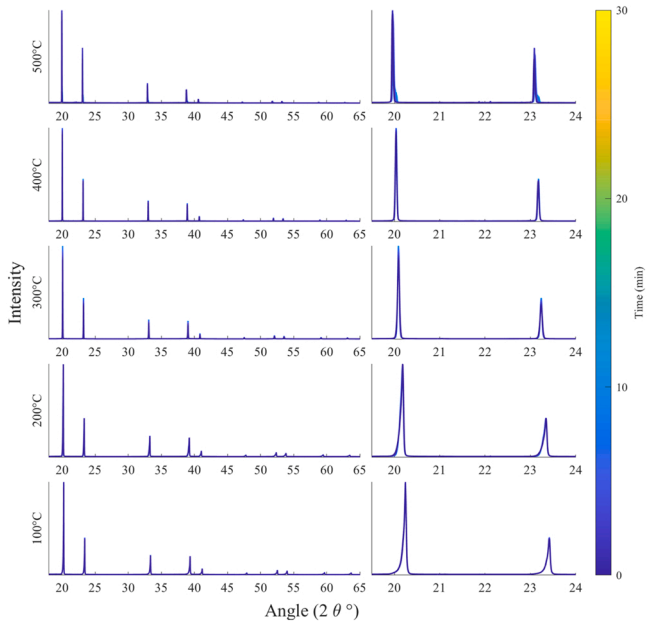

Fig. 16. Full (left) and low angle (right) XRD patterns of Scalmalloy sample at hold temperatures from 100 °C to 500 °C.

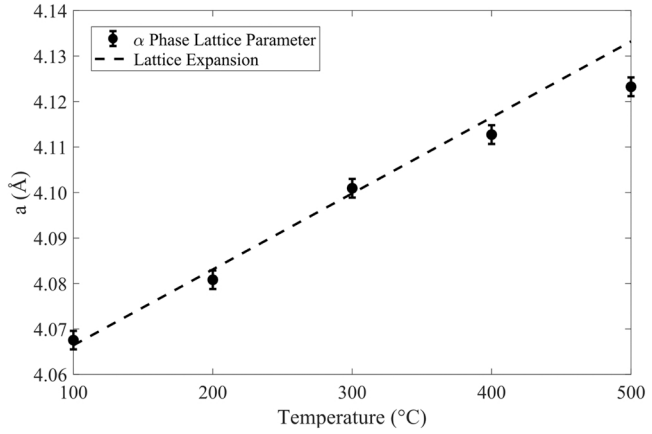

Fig. 17. Expansion of main α-Al phase lattice parameter at hold temperatures from 100 °C to 500 °C.

3.6. Discussion

The results presented provide insights into the mechanical properties of the most used materials in L-PBF AM at the powder scale, and are summarised in Fig. 18. In general red has been used to indicate factors which have a negative response on part performance. For example, for Ti64 this figure indicates that heating the particles above 500 °C is sufficient to relieve strain in the samples, but that holds at temperatures above 700 °C pose an oxidation risk. This suggests that the production process should be developed to ensure all particles remaining within the sample are heated above 500 °C, but that the time the sample is held above 700 °C should be minimised. This information is likely to be useful in the selection of annealing temperatures, but are aware that a large number of other factors need to be considered when determining optimal annealing programs.

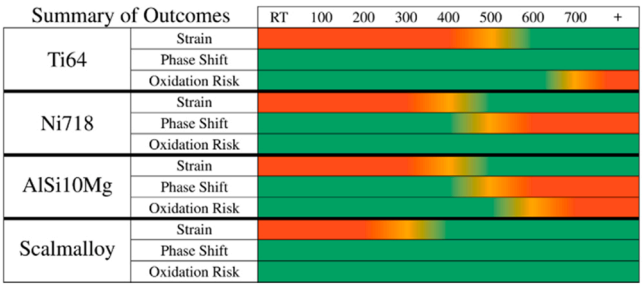

Fig. 18. Summary of effects related to temperature identified in this study, in general red regions refer to behaviour which has a negative response on part performance.

Fig. 18 demonstrates that phase transformation is not a large factor at this scale for L-PBF for any materials. This is likely due to design of these high-quality AM alloys which are effective at maintaining the mechanical integrity of the powder after production. In contrast, each material has some magnitude of internal stress induced due to the gas atomisation powder production process. Mitigations for relieving the internal stresses include using production methods such as plasma wire atomisation that yield finer powder volumes, heating the build plate during the L-PBF process to reduce the temperature gradient through the build chamber, or heat treating the parts to reach the required temperatures to relieve the stress as illustrated in Fig. 18. However, these methods will require a balance to optimise to the desired final part properties. Kaufmann et al. (2016) found no significant effect on part cracking from residual stresses in aluminium alloys when pre-heating the build plate to 200 °C [76] while Ali et al. (2017) found a reduction of residual stress in Ti64 by up to 70 % when pre-heating the build plate to 370 °C, 88 % at 470 °C, and no significant residual stress when the build plate was heated to 570 °C [77]. It is important to note that while any heat treatment on the constituent powder will reduce the residual stresses on the powder particles as specified in this study, the impact that any initial internal stress in the constituent powder has on the final part quality should be investigated further. The timescales at high temperatures investigated in this research were also longer than the powder in a build chamber would be exposed to elevated temperatures. While there were no significant changes to the powder structure at the hold temperatures, any effects of additional strain relief would be unlikely to occur during the build process. The samples that showed evolution in strain relief at a specific hold temperature were Ti64 at 500 °C and 600 °C, AlSi10Mg at 300 °C, and Scalmalloy at 300 °C. Despite the extended hold times compared to a typical AM build cycle, these data can be representative of the general response of the material powder. Despite being similar in nature, the temperatures, processing parameters, mechanical properties and thermal characteristics of the alloys under consideration mean that the fabrication processes for are substantially different. The exact nature of these processes are not publicly available due to the extensive investment required to optimise the routines (and associated IP). However, the magnitude and distribution of strain within the particles is a function of melting temperature (or ΔT to room temperature), thermal expansion coefficient, Young's modulus and thermal conductivity which are substantially different for all of the alloys examined in this study. This means that the magnitude and distribution of strain, and associated peak shapes are expected to vary substantially from one alloy to another, as observed experimentally.

Oxidation is still an issue at high temperatures and is difficult to avoid in L-PBF manufacturing, and has potentially two origins – oxides present within the pre-sintered powder or the incomplete removal of oxygen from the atmosphere within the chamber. Although signs of oxidised α phase were only seen in Ti64 and $AlSi_{10}Mg$ through the analysis in this study, the presence of surface oxides is still a key consideration in any L-PBF processes with materials reaching elevated temperatures. Simonelli et al. (2015) found selective surface oxidation in $AlSi_{10}Mg$, but no traces of oxidation in the bulk material microstructure in this alloy or in Ti64 [78]. As indicated by Grell et al. (2016), limiting oxidation in the final parts is key for structural integrity, as an increase of powder oxygen mass fraction from 0.11 % to 0.53 % was related to reduced impact toughness by a factor of up to 16 times [79].

While it was difficult to confirm the presence of oxidation, the characteristics found through this study in Ti64 and $AlSi_{10}Mg$ indicate that further investigation through additional techniques could provide insight in whether the powder production methods can lead to oxidised powder. Methods such as Scanning Electron Microscopy (SEM) could show the quality of the powder, and either confirm the quality for use or show which atomisation methods need further controls to eliminate the presence of oxides, although this was deemed beyond the scope of the present manuscript.

Awareness of how thermal cycles may impact powder properties may be especially relevant for monitoring part quality with increased powder reuse. During the L-PBF process, powder close to the laser source that is not being sintered may still reach temperatures near to its melting point, without any sintering, and therefore will still be small enough to be reused multiple times. This is especially critical for Ni718 or $AlSi_{10}Mg$ as the findings from this study show that there is approximately a 100 °C of temperature window between full internal strain relief in the powder grains and changing the mechanical properties through phase changes or oxidation in the case of the aluminium-based alloy. While the elevated temperatures required for melting will typically alleviate any induced internal strains in the powder, it is still important to consider the unsintered powder in these processes due to any partially sintered particles that are typically found on the surface of untreated builds. These unsintered powders could potentially lead to the propagation of fatigue cracks, as stress concentrations are typically located on the surface of components. Yi et al. (2021) showed the drop-off in the final part yield strength and elongation at break of Ni716 after at least 6 reuse cycles, with further reduction of strength after 14 cycles. However, there is no impact to the tensile strength of any of the final parts with multiple reuse cycles [80]. Additionally, Li et al. (2016) have shown a similar decrease in tensile strength of $AlSi_{10}Mg$ as-built specimens that have been heat treated at 550 °C for 2 h by approximately 250 MPa, however, the fracture strain after this treatment is increased by a factor of almost 5 times [81]. This is likely an effect of the phase change of the material which is also seen in the powder at a temperature above 500 °C. With their careful atmospheric control in combination with the increase in fracture strain of the heat-treated parts, there is unlikely to be any oxidation of the as-built part during this heat treatment process in the work by Li et al. (2016). It is therefore important for the final part quality to keep the constituent powder below critical temperatures that would lead to unwanted phase changes or oxidation and exposing powder to elevated temperatures to relieve internal lattice strain. "These critical regions are summarised by the desired regions in green in Fig. 18."

While the results from this experiment show that exposing the powder grains to high temperature can both relieve internal stresses and cause mechanical changes through phase shifts or oxidation, it is important to note that the conditions from this experiment are not wholly representative of traditional L-PBF conditions. One key difference includes the duration the material was held at each of the elevated temperatures. In L-PBF processes, the laser induces heat in the powder, and it remains at an elevated temperature for an order of seconds to minutes, whereas these powder samples were held at high temperatures for up to 30–60 min.

Future work related to this research will involve an investigation into different heat treatment methods on the microstructure of these AM powders, additional powder production methods in controlled atmospheric conditions, and complementary microscopy studies of these powders to gain a fuller understanding of the powder characteristics. These studies aim to help inform designers using additive manufacturing on the part quality from different conditions and to improve the production processes of AM powders to reduce the formation of precipitates and oxidisation. These results could form the basis of a new predictive functionality within the next generation of AM software, which is urgently required to maximise powder reuse and thereby minimise wastage, whilst conserving the mechanical integrity of AM parts. Finally, the use of the precipitate phase and oxide growth rates in atmospheres containing differing oxygen levels would be vital information in order to prescribe the atmospheric conditions required for reliable manufacture and feedstock reuse.

4. Conclusions

The findings from this paper highlight key production parameters for metal AM powders for four commonly used metal alloys. Such insights are critically needed to increase part quality and consistency after powder atomisation or to reliably determine the number of times a powder can be reused without degradation of part performance. With powder use, it is important to avoid any powder defects such as unwanted precipitation and phase changes, oxidation, or internal thermal stresses. Not only will these lead to potential inconsistent properties and defects in the powder, but this may compound to lead to potential build defects that lead to material wastage or part failure if undetected.

However, with these results, it is important to recognise that these temperatures were held for up to 60 min, whereas in practical AM processes, extreme high temperatures will be reached for significantly less time. As discovered through this paper's characterisation of AM powders, the Scalmalloy powder has the largest temperature range before the powder quality is impacted. This is due to the lower temperature required for strain relief and the minimal risk of worsening mechanical properties due to phase changes or oxidation. In materials with a lower thermal conductivity such as Ni718, the powder production methods and AM use due to powder reuse and build parameters are much more important as the lattice strain relief is more costly than in the aluminium-based alloys due to the lower required temperatures of roughly 300 °C which only need to be held for a shorter period of time versus the nickel alloys. This is also an important consideration in Ti64 due to its high susceptibility to generate large internal strains in the atomisation process which will also require high temperatures to relieve. These factors combined all highlight the importance of care in the early stages of powder production.

CRediT authorship contribution statement

Max Valentine: Formal analysis, Writing – original draft, Writing – review & editing, Visualization. **Vimal Dhokia**: Conceptualization, Supervision, Funding acquisition. **Joseph Flynn**: Investigation. **Sophie McNair**: Investigation. **Alexander Lunt**: Conceptualization, Methodology, Investigation, Writing – review & editing, Supervision, Project administration, Funding acquisition.

Declaration of Competing Interest

The authors declare the following financial interests/personal relationships which may be considered as potential competing interests: Alexander Lunt reports equipment, drugs, or supplies was provided by Diamond Light Source Ltd. Alexander Lunt reports equipment, drugs, or supplies was provided by Carpenter Powder Products AB. Alexander Lunt reports financial support was provided by Engineering and Physical Sciences Research Council.

Data Availability

The authors are unable or have chosen not to specify which data has been used.

Acknowledgements

The authors would like to thank Carpenter technology for providing the powder samples, Diamond Light Source for access to synchrotron X-ray diffraction with proposal number 23975, and Dr. Sarah Day and Dr. Chiu Tang for their assistance with the TOPAS structural Rietveld

refinements. We would also wish to acknowledge the use of the EPSRC funded Physical Sciences Data-science Service hosted by the University of Southampton and STFC under grant number EP/S020357/1.

References

[1] B. Li, et al., Electron beam freeform fabrication of NiTi shape memory alloys: crystallography, martensitic transformation, and functional response, Mater. Sci. Eng. A 843 (March) (2022), 143135.
[2] X. Zuo, et al., Wire-based directed energy deposition of NiTiTa shape memory alloys: Microstructure, phase transformation, electrochemistry, X-ray visibility and mechanical properties, Addit. Manuf. 59 (PB) (2022), 103115.
[3] B.P. Conner, et al., Making sense of 3-D printing: creating a map of additive manufacturing products and services, Addit. Manuf. 1–4 (2014) 64–76.
[4] S. Liu, Y.C. Shin, Additive manufacturing of Ti6Al4V alloy: a review, Mater. Des. 164 (2019), 107552.
[5] M. Tang, P.C. Pistorius, Oxides, porosity and fatigue performance of AlSi10Mg parts produced by selective laser melting, Int. J. Fatigue 94 (2017) 192–201.
[6] K. Dietrich, J. Diller, S. Dubiez-Le Goff, D. Bauer, P. Forêt, G. Witt, The influence of oxygen on the chemical composition and mechanical properties of Ti-6Al-4V during laser powder bed fusion (L-PBF), Addit. Manuf. 32 (2020), 100980.
[7] M. Awd, J. Tenkamp, M. Hirtler, S. Siddique, M. Bambach, F. Walther, Comparison of microstructure and mechanical properties of Scalmalloy® produced by selective laser melting and laser metal deposition, Mater. (Basel). 11 (1) (2017).
[8] L. Cordova, M. Campos, T. Tinga, Revealing the effects of powder reuse for selective laser melting by powder characterization, JOM 71 (3) (2019) 1062–1072.
[9] J.N. Rousseau, A. Bois-Brochu, C. Blais, Effect of oxygen content in new and reused powder on microstructural and mechanical properties of Ti6Al4V parts produced by directed energy deposition, Addit. Manuf. 23 (2018) 197–205.
[10] G. Soundarapandiyan, et al., The effects of powder reuse on the mechanical response of electron beam additively manufactured Ti6Al4V parts, Addit. Manuf. 46 (2021), 102101.
[11] L.C. Ardila, et al., Effect of IN718 recycled powder reuse on properties of parts manufactured by means of selective laser melting, Phys. Procedia 56 (C) (2014) 99–107.
[12] A. Montelione, S. Ghods, R. Schur, C. Wisdom, D. Arola, M. Ramulu, Powder reuse in electron beam melting additive manufacturing of Ti6Al4V: particle microstructure, oxygen content and mechanical properties, Addit. Manuf. 35 (2020), 101216.
[13] E.J. Garboczi, N. Hrabe, Particle shape and size analysis for metal powders used for additive manufacturing: Technique description and application to two gas-atomized and plasma-atomized Ti64 powders, Addit. Manuf. 31 (2020), 100965.
[14] I. Chang, Y. Zhao, 1.2 Atomisation techniques. Advances in Powder Metallurgy - Properties, Processing and Applications, Woodhead Publishing, 2013, pp. 5–9.
[15] A. Sunar Baskoro, S. Supriadi, Review on Plasma Atomizer Technology for Metal Powder.
[16] I. Chang, Y. Zhao, 1.3 Problems and advances in gas atomisation. Advances in Powder Metallurgy - Properties, Processing and Applications, Woodhead Publishing,, 2013, pp. 9–15.
[17] P. Moghimian, et al., Metal powders in additive manufacturing: a review on reusability and recyclability of common titanium, nickel and aluminum alloys, Addit. Manuf. vol. 43 (. 2021), 102017.
[18] I. Yadroitsev, I. Yadroitsava, Evaluation of residual stress in stainless steel 316L and Ti6Al4V samples produced by selective laser melting, Virtual Phys. Prototyp. (2015).
[19] T. Mukherjee, V. Manvatkar, A. De, T. DebRoy, Mitigation of thermal distortion during additive manufacturing, Scr. Mater. 127 (2017) 79–83.
[20] X. Lu, et al., Substrate design to minimize residual stresses in Directed Energy Deposition AM processes, Mater. Des. 202 (2021), 109525.
[21] S. Leuders, et al., On the mechanical behaviour of titanium alloy TiAl6V4 manufactured by selective laser melting: Fatigue resistance and crack growth performance, Int. J. Fatigue 48 (2013) 300–307.
[22] J.L. Bartlett, X. Li, An overview of residual stresses in metal powder bed fusion, Addit. Manuf. 27 (2019) 131–149.
[23] P. Edwards, A. O'Conner, M. Ramulu, Electron beam additive manufacturing of titanium components: properties and performance, J. Manuf. Sci. Eng. Trans. ASME 135 (2013) 6.
[24] J.H. Martin, B.D. Yahata, J.M. Hundley, J.A. Mayer, T.A. Schaedler, T.M. Pollock, 3D printing of high-strength aluminium alloys, Nature 549 (7672) (2017) 365–369.
[25] C.L.A. Leung, S. Marussi, M. Towrie, R.C. Atwood, P.J. Withers, P.D. Lee, The effect of powder oxidation on defect formation in laser additive manufacturing, Acta Mater. 166 (2019) 294–305.
[26] A.R. Balachandramurthi, J. Moverare, S. Mahade, R. Pederson, Additive manufacturing of alloy 718 via electron beam melting: Effect of post-treatment on the microstructure and the mechanical properties, Materials (Basel). 12 (1) (2018).
[27] S.I. Shakil, A. Hadadzadeh, B. Shalchi Amirkhiz, H. Pirgazi, M. Mohammadi, M. Haghshenas, Additive manufactured versus cast AlSi10Mg alloy: microstructure and micromechanics, Results Mater. 10 (2021), 100178.
[28] Carpenter Technology, "Ti 6Al-4V - Specialty Alloys." [Online]. Available: https://www.carpentertechnology.com/alloy-finder/ti-6al-4v. [Accessed: 10-May-2022].
[29] Carpenter Technology, "PowderRange 718 - Specialty Alloys." [Online]. Available: https://www.carpentertechnology.com/alloy-finder/powderrange-718. [Accessed: 10-May-2022].
[30] Carpenter Technology, "PowderRange AlSi10Mg - Specialty Alloys." [Online]. Available: https://www.carpentertechnology.com/alloy-finder/powderrange-alsi10mg. [Accessed: 10-May-2022].
[31] Carpenter Technology, "Scalmalloy - Specialty Alloys." [Online]. Available: https://www.carpentertechnology.com/alloy-finder/scalmalloy. [Accessed: 10-May-2022].
[32] S.P. Thompson, et al., Beamline I11 at Diamond: a new instrument for high resolution powder diffraction, Rev. Sci. Instrum. 80 (2009) 879.
[33] S.P. Thompson, et al., Fast X-ray powder diffraction on I11 at Diamond, J. Synchrotron Radiat. 18 (2011) 637–648.
[34] T.A. Rodrigues, et al., Effect of heat treatments on 316 stainless steel parts fabricated by wire and arc additive manufacturing: microstructure and synchrotron X-ray diffraction analysis, Addit. Manuf. 48 (PB) (2021), 102428.
[35] T.A. Rodrigues, et al., Wire and arc additive manufacturing of 316L stainless steel/Inconel 625 functionally graded material: Development and characterization, J. Mater. Res. Technol. 21 (2022) 237–251.
[36] V. Pecharsky, P. Zavalij. Fundamentals of Powder Diffraction and Structural Characterization of Materials, Second edition,, Springer, US, 2008.
[37] F.R. Kaschel, et al., Mechanism of stress relaxation and phase transformation in additively manufactured Ti-6Al-4V via in situ high temperature XRD and TEM analyses, Acta Mater. 188 (2020) 720–732.
[38] N. Baimpas, A.J.G. Lunt, I.P. Dolbnya, J. Dluhos, A.M. Korsunsky, Nano-scale mapping of lattice strain and orientation inside carbon core SiC fibres by synchrotron X-ray diffraction, Carbon N. Y 79 (1) (2014) 85–92.
[39] E. Bemporad, et al., A critical comparison between XRD and FIB residual stress measurement techniques in thin films, Thin Solid Films 572 (2014) 224–231.
[40] S. Malinov, W. Sha, Z. Guo, C.C. Tang, A.E. Long, Synchrotron X-ray diffraction study of the phase transformations in titanium alloys, Mater. Charact. 48 (4) (2002) 279–295.
[41] R. Pederson, Microstructure and Phase Transformation of Ti-6Al-4V," Lulea University of Technology, 2002.
[42] M. Basham, et al., Data analysis WorkbeNch (DAWN), J. Synchrotron Radiat. 22 (2015) 853–858.
[43] Diamond Light Source, "Welcome to I11." [Online]. Available: https://www.diamond.ac.uk/Instruments/Crystallography/I11.html. [Accessed: 07-Nov-2021].
[44] R.K. Kirby, Platinum—a thermal expansion reference material, Int. J. Thermophys. 12 (4) (1991) 679–685.
[45] B. Graybill, M. Li, D. Malawey, C. Ma, J.M. Alvarado-Orozco, E. Martinez-Franco, Additive manufacturing of nickel-based superalloys, ASME 13th Int. Manuf. Sci. Eng. Conf. 1 (2018).
[46] Y. Ma, D. Cuiuri, C. Shen, H. Li, Z. Pan, Effect of interpass temperature on in-situ alloying and additive manufacturing of titanium aluminides using gas tungsten arc welding, Addit. Manuf. 8 (2015) 71–77.
[47] S.Z. Uddin, L.E. Murr, C.A. Terrazas, P. Morton, D.A. Roberson, R.B. Wicker, Processing and characterization of crack-free aluminum 6061 using high-temperature heating in laser powder bed fusion additive manufacturing, Addit. Manuf. 22 (2018) 405–415.
[48] W. Guo, et al., Effect of laser shock processing on oxidation resistance of laser additive manufactured Ti6Al4V titanium alloy, Corros. Sci. 170 (2020), 108655.
[49] H.M. Rietveld, A profile refinement method for nuclear and magnetic structures, J. Appl. Cryst. 2 (1969) 65.
[50] A.A. Coelho, TOPAS and TOPAS-Academic: an optimization program integrating computer algebra and crystallographic objects written in C++, J. Appl. Crystallogr. 51 (2018) 210–218.
[51] S. Gražulis, et al., Crystallography open database - an open-access collection of crystal structures, J. Appl. Crystallogr. 42 (4) (2009) 726–729.
[52] S. Gražulis, et al., Crystallography Open Database (COD): an open-access collection of crystal structures and platform for world-wide collaboration, Nucleic Acids Res. 40 (D1) (2012) D420–D427.
[53] A. Vaitkus, A. Merkys, S. Gražulis, Validation of the crystallography open database using the crystallographic information framework, J. Appl. Crystallogr. 54 (2) (2021) 661–672.
[54] K.D.M. Harris, M. Tremayne, Crystal structure determination from powder diffraction data, Chem. Mater. 8 (1996) 2554–2570.
[55] M. Johnson, L. Eriksson, Thermal expansion of Al and TiB2 in the temperature range 300 to 900 K and calculated lattice fit at the melting temperature for Al, Int. J. Mater. Res. 89 (7) (1998) 478–480.
[56] D. Siebörger, H. Brehm, F. Wunderlich, D. Möller, U. Glatzel, Temperature dependence of lattice parameter, misfit and thermal expansion coefficient of matrix, γ′ phase and superalloy, Int. J. Mater. Res. 92 (1) (2001) 58–61.
[57] M. Yakout, M.A. Elbestawi, S.C. Veldhuis, S. Nangle-Smith, Influence of thermal properties on residual stresses in SLM of aerospace alloys, Rapid Prototyp. J. vol. 26 (1) (. 2020) 213–222.
[58] V.V. Popov, et al., Powder bed fusion additive manufacturing using critical raw materials: a review, Materials (Basel) 14 (4) (2021) 909.
[59] K. Somlo, K. Poulios, C.V. Funch, C.F. Niordson, Anisotropic tensile behaviour of additively manufactured Ti-6Al-4V simulated with crystal plasticity, Mech. Mater. 162 (2021), 104034.
[60] M. Levitsky, B.W. Shaffer, Residual thermal stresses in a solid sphere cast from a thermosetting material, J. Appl. Mech. 42 (3) (1975) 651–655.
[61] M. Albu, R. Krisper, J. Lammer, G. Kothleitner, J. Fiocchi, P. Bassani, Microstructure evolution during in-situ heating of AlSi10Mg alloy powders and additive manufactured parts, Addit. Manuf. 36 (2020), 101605.
[62] R. Pederson, O. Babushkin, F. Skystedt, R. Warren, Use of high temperature X-ray diffractometry to study phase transitions and thermal expansion properties in Ti-6Al-4V, Mater. Sci. Technol. 19 (11) (2013) 1533–1538.

[63] G. Lütjering, Influence of processing on microstructure and mechanical properties of (α+β) titanium alloys, Mater. Sci. Eng. A 243 (1–2) (1998) 32–45.
[64] M.G. Kotresh, M.K. Patil, S.R. Inamdar, Reaction temperature based synthesis of ZnO nanoparticles using co-precipitation method: detailed structural and optical characterization, Optik (Stuttg) 243 (2021), 167506.
[65] F. Whba, F. Mohamed, N.R.A. Md Rosli, I. Abdul Rahman, M.I. Idris, The crystalline structure of gadolinium oxide nanoparticles (Gd2O3-NPs) synthesized at different temperatures via X-ray diffraction (XRD) technique, Radiat. Phys. Chem. 179 (2021), 109212.
[66] M.T. Izumi, et al., In situ X-ray diffraction analysis of face-centered cubic metals deformed at room and cryogenic temperatures, J. Mater. Eng. Perform. 28 (8) (2019) 4658–4666.
[67] R.M. Nunes, D. Pereira, T. Clarke, T.K. Hirsch, Delta phase characterization in inconel 718 alloys through x-ray diffraction, ISIJ Int. 55 (11) (2015) 2450–2454.
[68] T. Ungár, Dislocation densities, arrangements and character from X-ray diffraction experiments, Mater. Sci. Eng. A 309–310 (2001) 14–22.
[69] T. Ungár, Microstructural parameters from X-ray diffraction peak broadening, Scr. Mater. 51 (8) (2004) 777–781.
[70] J. Lohmiller, R. Baumbusch, O. Kraft, P.A. Gruber, Differentiation of deformation modes in nanocrystalline Pd films inferred from peak asymmetry evolution using in situ X-ray diffraction, Phys. Rev. Lett. 110 (6) (2013) 66101.
[71] A.M. Afanas'ev, R.M. Imamov, E.K. Mukhmedzhanov, Asymmetric X-Ray diffraction, Crystallogr. Rev. 3 (2) (1992) 157–226.
[72] K. Venkateswarlu, A. Chandra Bose, N. Rameshbabu, X-ray peak broadening studies of nanocrystalline hydroxyapatite by Williamson–Hall analysis, Phys. B Condens. Matter 405 (20) (2010) 4256–4261.
[73] C. Yu, et al., Synchrotron high energy X-ray diffraction study of microstructure evolution of severely cold drawn NiTi wire during annealing, Acta Mater. 115 (2016) 35–44.
[74] X. Liu, C. Zhao, X. Zhou, Z. Shen, W. Liu, Microstructure of selective laser melted AlSi10Mg alloy, Mater. Des. 168 (2019), 107677.
[75] M. Rafieazad, M. Mohammadi, A.M. Nasiri, On microstructure and early stage corrosion performance of heat treated direct metal laser sintered AlSi10Mg, Addit. Manuf. 28 (2019) 107–119.
[76] N. Kaufmann, M. Imran, T.M. Wischeropp, C. Emmelmann, S. Siddique, F. Walther, Influence of process parameters on the quality of aluminium alloy en AW 7075 using Selective Laser Melting (SLM), Phys. Procedia 83 (2016) 918–926.
[77] H. Ali, L. Ma, H. Ghadbeigi, K. Mumtaz, In-situ residual stress reduction, martensitic decomposition and mechanical properties enhancement through high temperature powder bed pre-heating of Selective Laser Melted Ti6Al4V, Mater. Sci. Eng. A 695 (2017) 211–220.
[78] M. Simonelli, et al., A study on the laser spatter and the oxidation reactions during selective laser melting of 316L stainless steel, Al-Si10-Mg, and Ti-6Al-4V, Metall. Mater. Trans. A Phys. Metall. Mater. Sci. 46 (9) (2015) 3842–3851.
[79] W.A. Grell, et al., Effect of powder oxidation on the impact toughness of electron beam melt Ti-6Al-4V, Orig. Artic. 23 (2016).
[80] F. Yi, Q. Zhou, C. Wang, Z. Yan, B. Liu, Effect of powder reuse on powder characteristics and properties of Inconel 718 parts produced by selective laser melting, J. Mater. Res. Technol. 13 (2021) 524–533.
[81] W. Li, et al., Effect of heat treatment on AlSi10Mg alloy fabricated by selective laser melting: microstructure evolution, mechanical properties and fracture mechanism, Mater. Sci. Eng. A 663 (2016) 116–125.